Zeitschrift: Helvetica Physica Acta

Band: 69 (1996)

Heft: Sep. 1

Vereinsnachrichten: Réunion de printemps de la Société Suisse de Physique = Frühjahrstagung der Schweizerischen Physikalischen Gesellschaft = Spring meeting of the Swiss Physical Society

Autor: [s.n.]

Réunion de Printemps de la Société Suisse de Physique

Frühjahrstagung der Schweizerischen Physikalischen Gesellschaft

Spring Meeting of the Swiss Physical Society

March 7 and 8, 1996

Fribourg, Switzerland

Helv Phys Acta
Vol. 69, Separanda 1 (1996)

0018-0238/96/0100S1-02$1.50+0.20/0

TIME-OF-FLIGHT SECONDARY ION MASS SPECTROMETRY: A NEW VERSATILE TOOL FOR SURFACE ANALYSIS

B.A.KELLER

Swiss Federal Laboratories for Materials Testing and Research
CH-8600 Dübendorf/Switzerland

Time-of-flight secondary ion mass spectrometry (TOF-SIMS) is developing into one of the most significant and versatile analytical techniques for characterizing surface species of inorganic, organic and biological materials. Together with the option of imaging the surface chemistry, SSIMS provides specific chemical information which is complementary to structural data from infrared vibrational spectroscopy (FTIR) and elemental or chemical shift information from electron spectroscopy (ESCA).

Surface phenomena are important in diverse technological areas, such as adhesion, biocompatibility, catalysis or composite research. Most of the critical parameters are governed by the chemical composition of the uppermost monolayers of the solid. In many cases recent developments in the field of surface analysis have opened new pathways towards tailor-made surfaces. Since most of the technological important materials are of organic nature, the demand for detailed molecular information has become vital for the controlled modification of surfaces with respect to their adhesion, friction, wettability or biocompatibility properties. The chemical characterization of surfaces usually demands answers to the nature, location and concentration of the molecular species present ('what is it, where is it, and how much').

Among the analytical techniques most commonly used for obtaining molecular information of surfaces are X-ray photoelectron spectroscopy (XPS, or ESCA) and surface mass spectrometry. Methods like Auger spectrometry, or the more recent scanning probe techniques (STM, AFM) are not suitable to provide this information.

The emission of secondary particles upon impinging of a primary ion beam with an energy on the order of several keV has been widely used in the past to analyze depth profiles of technological samples. However, because of the sputtering process involved in the formation of this primary ion-induced formation of secondary particles, the surface under investigation is loosing its native chemical composition during the course of the analytical process. It has been recognized by Benninghoven [1] that static SIMS conditions can be maintained over the measurement process by keeping the ion dose $< 10^{13}$ ions/cm^2. After the primary ion strikes the surface, most of its energy is transferred by a nuclear stopping process during hard sphere collisions. In the near-surface region, knock-on collision cascades are dominating, but part of the primary ion's energy is dissipated into the bulk, causing displacement collisions. Some of the cascades can return to the surface, giving rise to the emission of secondary particles with an energy of approximately 20-25 eV and a chemical

composition which is characteristic for the species present at the surface. In the TOF-SIMS technique, positively or negatively charged ions are accelerated into the field free region of a reflectron type mass analyzer with known length in which they are separated according to their mass and recorded in a time-to-digital converter. In order to measure the different arrival times, either the primary ion gun or the extraction optics of the analyzer has to be pulsed. In a typical pulsed acquisition cycle, 1-10 secondary ions are detected. Therefore, a large number of cycles has to be accumulated to obtain a mass spectrum with good signal-to-noise ratio [2,3].

The advantages of the TOF-SIMS technique over older systems based on quadrupole analyzers are the greater sensitivity, mass range and resolution. Except some very special microprobes, the more conventional instruments are also not allowing to raster the primary ion beam to obtain images of the lateral distribution of the surface species. This last feature is unique for TOF-SIMS instruments with respect to the mapping the chemical composition of organic surfaces in the µm-range.

Although magnetic sector and quadrupole mass spectrometers have the potential to generate static SIMS spectra, they are usually limited by mass range, mass resolution and sensitivity. Due to the introduction of the reflectron technology in TOF-SIMS spectrometers, modern instruments of this type are now routinely reaching mass resolutions of $m/\Delta m > 9000$ at $m/z=28$, enabling the separation of signals C_nH_m and $C_{n-1}H_{m-4}O$ with a necessary mass resolution of $m/\Delta m=800$ at mass $m/z=28$ and $m/\Delta m=1500$ at $m/z=55$, respectively. The problem of distinguishing between these types of signals is common in analyzing plasma or corona modified polymer surfaces with improved adhesion properties. Another demanding task is the separation between signals arising from Fe^+ and Si_2^+ at mass $m/z=56$. The broad mass range of the flight time analyzer is a key feature for the detection of larger fragments which are typical in adhesion, polymer science and biocompatibility studies. The possibility of kV post acceleration of the secondary ions allows the detection of mass fragments up to several thousand Dalton. Particularly in the filed of polymer science the identification of end groups [4], additives and organic contaminants like siloxanes is important for mapping out failure mechanisms. Interface debonding caused by weak boundary layers of incompatible surface species is a common problem in adhesion science.

Among the various applications of chemical imaging of surfaces are the mapping of sensor surfaces, microelectronic components (e.g. GaAs) and organic coatings. From the distribution of drug components in cross-sectioned micro pills to car paint corrosion blisters and even native biological samples, the versatility the TOF-SIMS technique as a complementary analytical tool to the long known XPS instruments clearly broadens the possibilities of surface characterization in materials science.

[1] A.Benninghoven, Z.Physik **230**, 403 (1970)
[2] R.J.Cotter, Anal.Chem. **64**, 1027A (1992)
[3] J.C.Vickerman, A.Brown and N.M.Reed, Secondary Ion Mass Spectrometry(Oxford Science Publications, Oxford 1989)
[4] B.A.Keller, D.Weber and H.-P.Brack, Surf.Interface Anal. (1996),in print

Helv Phys Acta
Vol. 69, Separanda 1 (1996)

0018-0238/96/0100S3-02$1.50+0.20/0

Preparation and characterization of rhombohedral PZT thin films

M. Foeth[1], A. Sfera[1], J.-M. Triscone[2], Ø. Fischer[2], P. Stadelmann[1], P. A. Buffat[1]

[1] Centre Interdépartemental de Microscopie Electronique, EPFL, 1015 Lausanne, Switzerland
[2] Département de Physique de la Matière Condensée, University of Geneva, 1211 Geneva 4, Switzerland

Epitaxial ferroelectric PZT (lead zirconium titanate $Pb(Zr_{0.6}Ti_{0.4})O_3$) thin films, that display a second order phase transition, have been produced on (100) $SrTiO_3$ substrates. The films, grown by off-axis RF magnetron sputtering, are uniform over large areas. Different x-ray diffraction techniques (Θ–2Θ, rocking curve and Φ-scan) reveal the high crystalline quality and strong epitaxial character of the films. Transmission electron microscopy (TEM) is used to characterize the roughness of the PZT/$SrTiO_3$ interfaces as well as their epitaxial behavior. TEM will also be used to study the ferroelectric domain wall properties close to the Curie point.

Some ferroelectric materials such as rhombohedral lead zirconium titanate $Pb(Zr_{0.6}Ti_{0.4})O_3$ (PZT) display a second order ferroelectric to paraelectric phase transition. In the ferroelectric state, the material is divided into domains of uniform spontaneous polarization, separated by domain walls. It has been shown that close to a critical point, the behavior of interfaces of two-dimensional systems differs drastically from that of three-dimensional systems, in particular it has been shown [1] that, unlike in three or more dimensions of space, the critical exponent describing the divergence of the interfacial thickness at a critical point is a non-universal function of the external field in contrast to the commonly accepted view that in the critical region, the interfacial thickness is proportional to the spontaneous fluctuations in the coexisting bulk phase. Unfortunately, experimental results are only available for three-dimensional systems.

With the idea to study a two-dimensional case, we produced rhombohedral PZT thin films in which we want to measure the domain wall thickness as a function of temperature by different transmission electron microscope (TEM) techniques such as high resolution transmission electron microscopy, electron holography and convergent beam electron diffraction (CBED).

In a first step, we prepared the ferroelectric thin films and analyzed their crystalline quality and epitaxial behavior by x-ray diffraction and TEM. The films were grown on (100) $SrTiO_3$ substrates by 90° off-axis RF magnetron sputtering with a substrate temperature of 540°C in an atmosphere of 30% oxygen and 70% argon at 200 mTorr [2]. The deposition rate is approximately 350Å per hour and the deposition is homogeneous over an area of about 3 cm x 3 cm.

The films of 10-200 nm thickness where then examined by x-ray diffraction. On Θ–2Θ diffractograms, the (001) and (002) reflections of PZT can be seen along with the (100) and (200) reflections of the substrate. The PZT peaks are extremely intense and narrow. The lattice parameter of PZT is found to be about 4.08Å which is consistent with previously reported thin film data [3]. The rocking curve full width at half maximum (FWHM) around the (001) reflection of PZT is 0.19° in comparison to FWHM values of 0.08°-0.09° for the single crystal $SrTiO_3$ substrate. We performed Φ-scans (azimuthal scans) on off-axis planes to analyze the epitaxial character of the films. Figure 1 shows the (110) $SrTiO_3$ and (011) PZT reflections for an azimuthal angle χ of 45°. Both, the substrate and the PZT exhibit a fourfold symmetry, the peaks are respectively aligned and very narrow which reveals a 'cube on cube' growth of the PZT films on the substrate and demonstrates a strongly epitaxial behavior.

TEM diffractions confirm the orientation of the films in the (001) direction as well as the lattice parameter value for the PZT thin film (4.08Å). Bright field and dark field TEM images show that the thickness of the film is homogeneous. A structure of vertical lines going from the substrate to the surface of the film, appear in regular distances of about 10-40 nm (Figure 2). Those lines could be a first indication for ferroelectric domain boundaries, but no further evidence can be given at this point. Possible reasons for the wave-like contrasts that can be seen at the interface, might be interfacial strain, domain adaptation or charge accumulation. High resolution transmission electron micrographs reveal that the $SrTiO_3$/PZT interface is very sharp and confirm that the PZT film is well aligned on the substrate lattice in the (001) direction.

In conclusion we successfully prepared PZT thin films by RF magnetron sputtering. Extensive x-ray analysis reveal the high crystalline quality and demonstrate the epitaxial growth of the films. TEM analysis confirms the crystalline quality and give a first indication for the presence of ferroelectric domains.

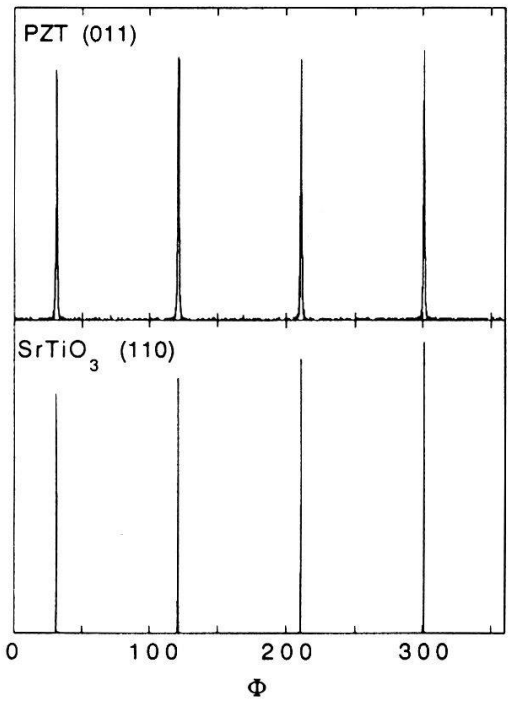

Figure 1: Φ-scan on PZT (011) and $SrTiO_3$ (110) planes

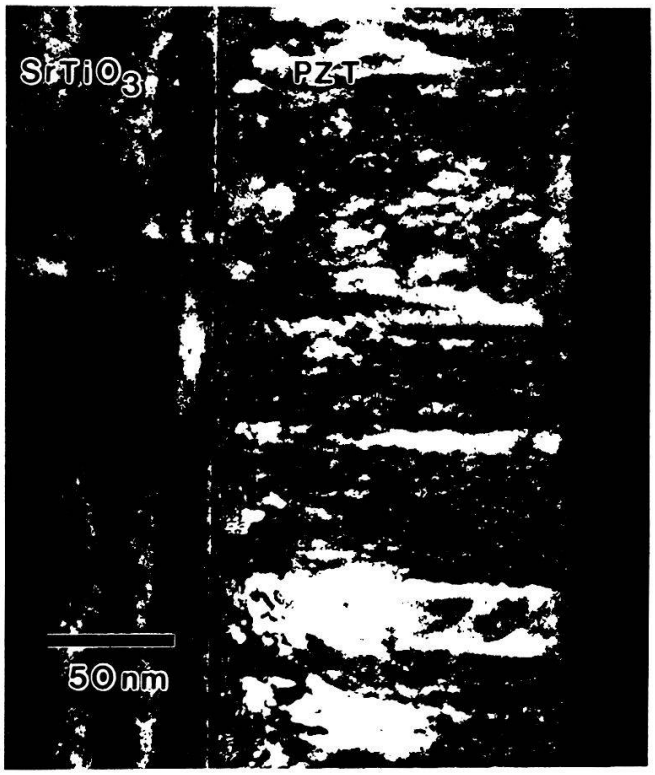

Figure 2: Dark field image of a PZT thin film on $SrTiO_3$

References

[1] M. Knackstedt and M. Robert, J. Chem. Phys. **89** (6), (1988)
[2] J.-M. Triscone et *al.*, J. Appl. Phys., to appear in april 1996
[3] R. Takayama and Y. Tomita, J. Appl. Phys. **65** (4), 15 February 1989

Helv Phys Acta
Vol. 69, Separanda 1 (1996)

0018-0238/96/0100S5-02$1.50+0.20/0

Anwendung der Oberflächenionisation in abbildenden Spektrometern in der Raumforschung

R. Schletti, P. Wurz, M.R. Aellig, P. Bochsler

Physikalisches Institut, Universität Bern, Sidlerstrasse 5, 3012 Bern

Oberflächenionisation ist eine in der Raumforschung noch nicht erprobte Methode. Oberflächen mit tiefer Austrittsarbeit vermögen niederenergetische Atome sehr effizient in negative Ionen umzuladen. Abbildende Spektrometer in der Magnetosphärenforschung benötigen eine solch effiziente Ionisation, denn die Flüsse von Neutralteilchen, die es zu messen gilt, sind für die Anwendung anderer Ionisationsmethoden zu gering.
Die Messung an verschiedenen Oberflächen mit niedriger Austrittsarbeit zeigen, dass Ionisationseffizienz, Langzeitstabilität, UV-Beständigkeit und Abbildungsvermögen den Anforderungen für den Einsatz in der Raumforschung genügen.

In der heutigen Magnetosphärenforschung werden die zahlreichen *in situ* Messungen allmählich durch Fernerkundungs-Messungen abgelöst. Diese sind für ein globales Verständnis der dynamischen Prozesse in der Magnetosphäre unendbehrlich. Niederenergetische (10 eV - 1 keV) Plasmateilchen (H, He und O), die durch Ladungsaustausch mit exosphärischem Gas neutralisiert werden und von den elektromagnetischen Feldern unbeeinflusst ballistischen Bahnen folgen, können von einem Satelliten aus mit einem abbildenden Massenspektrometer nach Masse, Energie und Einfallsrichtung analysiert werden [1], [2]. Da die Neutralgas-Flüsse sehr klein sind und eine hohe Zeitauflösung angestrebt wird, wird eine hocheffiziente Ionisationsmethode wie die Oberflächenionisation benötigt.

Bei der Oberflächenionisation werden Neutralteilchen durch Reflexion an einer metallischen Oberfläche niedriger Austrittsarbeit negativ gladen. Die Energie des Affinitätszustands der Teilchen wird durch das Bildladungspotential des Metalls verrigert. Nahe an der Oberfläche wird der in der Energie verbreiterte Affinitätszustand durch tunnelnde Metallelektronen besetzt.

In Abb. 1 ist der zeitliche Verlauf der Ionisationseffizienz eines 400 eV H_2-Stahls der unter 82° zur Normalen an einen bariumbeschichteten Wolframeinkristall(110) reflektiert wurde, gezeigt. Durch die Adsorption von Restgas (P = 10^{-7} mbar) erhöht sich die Austrittsabeit der Oberfläche und die Ionisationseffizienz nimmt von anfänglich etwa 7 % innerhalb eines Tages auf etwa 4 % ab. Es ist ersichtlich, dass mithilfe der Austrittsarbeit, die im Flug mit einer Leuchtdiode photoelektrisch gemessen werden kann, die momentane Ionisationseffizienz bestimmt werden kann. Nach einer Woche können noch negative Ionen nachgewiesen werden. Deshalb ist die Rekonditionierung der Oberfläche im Flug durch Ausheizen und anschliessendes Bedampfen nicht häufiger als ca. alle 10 Tage durchzuführen, zumal der Restgasdruck auf einem Satelliten um mindestens eine Grössenordnug tiefer ist.

In Abb. 2 ist das Strahlprofil nach der Reflexion an der Oberfläche gezeigt. Die Bedingungen waren die gleichen wie bei der Effizienzmessung. Die Strahldivergenz (FWHM) beträgt in polarer Richtung 9° und in azimutaler Richtung 8°. Für steilere Einschusswinkel

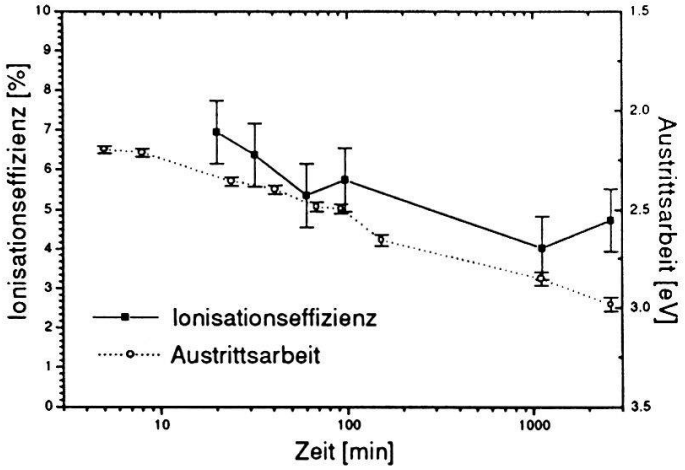

Abb. 1: Zeitlicher Verlauf der Ionisationseffizienz und der Austrittsarbeit.

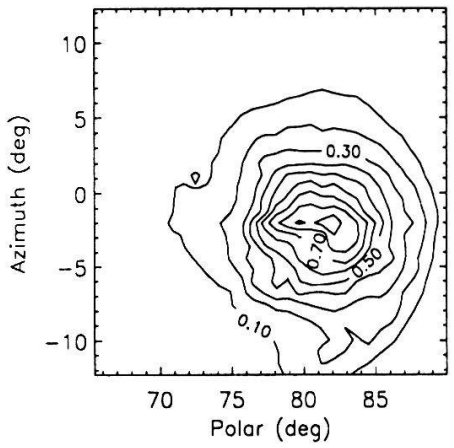

Abb. 2: Strahldivergenz nach Reflexion unter 82°.

	Cs/W110	Ba/Mo	Ba/W110
Ionisations Effizienz			
für H_2 400 eV 82° nach 10 Min	~ 10 %	~ 7 %	~ 7 %
für O_2 82° nach 10 Min.	~ 30 % (225 eV)	~ 35 % (400 eV)	~ 28 % (770 eV)
für H_2 400 eV 82° nach 1 Tag	~ 2 %	~ 4 %	~ 4 %
für O_2 82° nach 1 Tag	~ 10 % (225 eV)	~ 25 % (400 eV)	~ 20 % (770 eV)
UV-Beständigkeit	gut	gut	gut
Strahldivergenz			
für H_2 400 eV 82° FWHM			
polar	7°	~ 30°	9°
azimutal	8°	~ 10°	8°

Tabelle 1: Eigenschaften der untersuchten Oberflächen

nimmt die Strahldivergenz zu. In einem abbildenden Spektrometer wird der Teilchenstahl nach der Ionisation an der Oberfläche mit einem elektrostatischen Linsensystem gebündelt. Dabei muss die Streuung muss so gering wie möglich gehalten werden. Bei polykristallinem Molybdän als Substrat wurden Strahldivergenzen um 30° gemessen.

Messungen des zeitlichen Verlaufs der Austrittsarbeit unter intensiver UV-Bestrahlung (10 mal intensiver als die solare UV-Strahlung) zeigten keine wesentlichen Veränderungen gegenüber dem Verlauf ohne UV-Exposition. Nach einigen Stunden lag die Austrittsarbeit der bestrahlten Probe sogar tiefer, weil adsorbiertes Restgas desorbiert wird. Die untersuchten Oberflächen sind gegenüber UV-Strahlung stabil.

In Tabelle 1 ist eine Zusammenfassung der wichtigsten Resultate gegeben [3]. Sie zeigen, dass Oberflächenionisation für die Anwendung in Raumforschungsexperimenten geeignet ist, und dass Barium auf Wolfram(110) als Oberfläche vorzügliche Eigenschaften besitzt.

Referenzen

[1] A.G. Ghielmetti et al., Opt.Eng. 33, (1994), 362-370
[2] P. Wurz et al., Opt.Eng. 34, (1995), 2365-2376
[3] R. Schletti, Lizentiatsarbeit, Universität Bern (1996)

Helv Phys Acta
Vol. 69, Separanda 1 (1996)

0018-0238/96/0100S7-02$1.50+0.20/0

Stark Effect Measurements on Single Perylene Molecules

Marco Pirotta, Alois Renn, and Urs P. Wild

Laboratorium für Physikalische Chemie, ETH Zürich, 8092 Zürich, Schweiz

Fluorescence excitation spectra of single perylene molecules embedded in the Shpol'skii matrix n-nonane have been investigated at 1.7 K. On a time scale which is considerably larger than the triplet lifetime of the molecule, discrete spectral jumps of the single molecular absorption lines are observed. To investigate this jump behaviour, fluorescence excitation spectra at different applied electric field strengths to the sample have been recorded. From the resulting Stark shifts and the spectral jumps a maximum distance between the molecules and disturbing two-level systems can be estimated.

Fluorescence excitation and emission spectroscopy of single molecules (SMS) is an ideal source for the studies of guest-host interactions. In contrast to the "conventional" optical spectroscopy on bulk samples, SMS supplies physical information from one single species without averaging over a whole ensemble of molecules. Small changes on the spectral position of the absorption profile are no longer hidden under the inhomogeneous distribution, the single molecule serves as a probe on the nanometer scale. Different experiments monitored the changing of the single molecular absorption line upon application of external perturbations, such as hydrostatic pressure [1] or an electric field [2], [3]. In the following we will focus onto the Stark effect of the system perylene in n-nonane, which is a poly-crystalline Shpol'skii matrix at 1.7 K.

The sample preparation and the basic SMS setup is discussed elsewhere [4]. The sample was sandwiched between to microscope cover glasses which have been coated with optically transparent ITO layers at the outer sides. The applied homogeneous electric field component was parallel to the propagation direction of the laser light. The maximum applied field strength was ±6.7 kV/cm, and the total laser scan range was 12.1 GHz.

The Stark effect manifests as the displacement of the absorption line of a molecule upon applying an electric field. The figure shows a 2-dimensional Stark effect experiment with a horizontal mirror symmetry axis (dashed line) which is due to the continuous up and down scanning of the electric field. The lines represent the shifting excitation profiles of single molecules. The brighter a line is, the stronger was the molecular fluorescence. The dark regions represent background areas where no molecules could be excited. All the traces show a linear dependence between the absorption position and the applied electric field. The strong internal fields caused by the matrix break the symmetry and result in an induced dipole moment difference $\Delta\mu_{ind}$ between the ground and excited state. The slope ζ of the Stark shift is defined in (eq 1). It depends on the projection $\Delta\mu_E$ of the induced dipole moment μ_{ind} onto the electric field vector.

$$\zeta = \frac{\Delta\nu}{\Delta E} = -\frac{f_e}{h} \cdot \Delta\mu_E \qquad \text{(eq 1)}$$

$f_e = 1.35$ is an isotropic Lorentz field correction for the field inside the n-nonane matrix.

Most of the stark shifts were in the range $0\ \text{MHz} \cdot \text{cm} / \text{kV} \leq |\zeta| \leq 200\ \text{MHz} \cdot \text{cm} / \text{kV}$, the

largest stark shift values were $|\zeta| = 400$ MHz · cm / kV . According to (eq 1) this corresponds to a largest dipole moment difference along the electric field vector of $\Delta\mu_E = 0.58$D . No quadratic Stark effect, which one would expect for centro-symmetric molecules such as perylene, was observed at these low applied field strength.

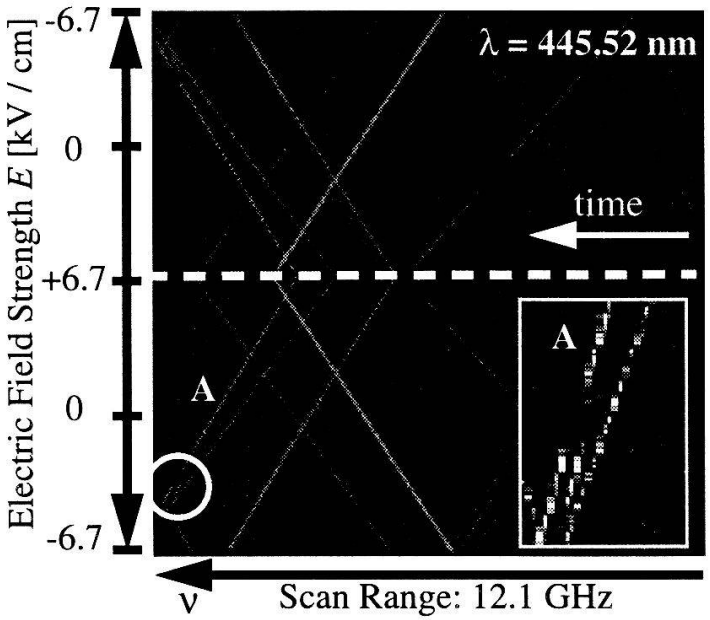

Figure 1: Molecular linear Stark effect traces.

The circle in the figure 1 shows a region where the molecular absorption line of the trace labelled with "A" has suddenly shifted to a different value. A few scans later, it jumped back to the "old" position. Spectral jumping, well known in SMS [5], could not be observed *directly* with other spectroscopic techniques in bulk samples. As a simple model it is assumed that the molecules interact with a so called two-level system (TLS) in the vicinity. The observed jump (see inset) was $\Delta\nu = 160$ MHz and $\Delta E = 780$ V/cm on the electric field axis respectively. An estimation of a maximal possible distance between the molecule and the disturbing TLS can be performed assuming electrostatic dipole-dipole interaction. The magnitude of the change in the electric field ΔE generated by a dipole moment μ_{TLS} at a distance r is given by:

$$\Delta E = \frac{2 \cdot \mu_{TLS}}{4\pi\varepsilon_0 \cdot r^3} \qquad \text{(eq 2)}$$

The displacement of a C-H bond of a nearby n-nonane molecule with a dipole moment of $\mu_{TLS} = \mu_{C-H} \cong 0.4$ D [6] might be a possible source for a TLS. Inserting this value into (eq 2) results in a maximal distance between the two interacting dipoles of $r_{max} = 6.7$ nm . This would approximately correspond to seven times the length and nine times the width of a single perylene molecule and seems to be quite large. However, it has to be emphasized that this is the *maximal* possible distance, that means, all dipole moments have to be parallel with respect to each other before the jump and the dipole of the TLS has to reverse its direction.

References

[1] M. Croci, H. J. Müschenborn, F. Güttler, A. Renn and U. P. Wild, Chem. Phys. Lett. **1,2**, 71 (1993).

[2] U.P. Wild, F. Güttler, M. Pirotta, and A. Renn, Chem. Phys. Lett. **193**, 451 (1992).

[3] M. Orrit, J. Bernard, A. Zumbusch, and R.I. Personov, Chem. Phys. Lett. **196**, 595 (1992).

[4] M. Pirotta, A. Renn, M. H. V. Werts, and U.P. Wild, Chem. Phys. Lett. (1996), in press.

[5] For the latest review see: L. Kador, Phys. Stat. Sol. (B) **189,** 11 (1995).

[6] A.E. Reed and F. Weinhold, J. Chem. Phys. **84**(4), 2428 (1986).

Financial support by the Swiss National Science Foundation is gratefully acknowledged.

Helv Phys Acta
Vol. 69, Separanda 1 (1996)

0018-0238/96/0100S9-02$1.50+0.20/0

ANALYTICAL CALCULATION OF PRANDTL'S MIXING LENGTH IN A TURBULENT AXI-SYMMETRIC JET

PETER W. EGOLF
Swiss Federal Laboratories for Materials Testing and Research, CH-8600 Dübendorf, Switzerland

DANIEL A. WEISS
Laboratoire PMMH, École Supérieure de Physique et de Chimie Industrielles de la Ville de Paris, F-75231 Paris, Cedex 05, France

Taking the difference quotient turbulence model into consideration, the production rate of turbulent kinetic energy of a round jet can be calculated. By a Fourier transformation the size of the eddies - which extract energy from the mean velocity field - has been determined. The bounding wave length is almost identical to Prandtl's mixing length.

In the equation describing the alteration of the turbulent kinetic energy in an axi-symmetric jet, the term which describes the mean energy transfer from the mean velocity field to the fluctuations is (e.g. see Ref. [1])

$$\dot{\varepsilon} = -\overline{u_2' u_1'} \cdot \frac{\partial \bar{u}_1}{\partial x_2} - \overline{u_1'^2} \cdot \frac{\partial \bar{u}_1}{\partial x_1} - \overline{u_2'^2} \cdot \frac{\partial \bar{u}_2}{\partial x_2} \cong -\overline{u_2' u_1'} \cdot \frac{\partial \bar{u}_1}{\partial x_2}. \tag{1}$$

If the difference-quotient turbulence model [2] is taken into consideration - for the production rate - the following result is obtained

$$\dot{\varepsilon} = \frac{u_0^3 \cdot x_0^3}{x_1^4} \cdot \left[\exp\left(-\frac{x_2^2}{b^2} \right) - \exp\left(-\frac{3}{2} \frac{x_2^2}{b^2} \right) \right] \geq 0. \tag{2}$$

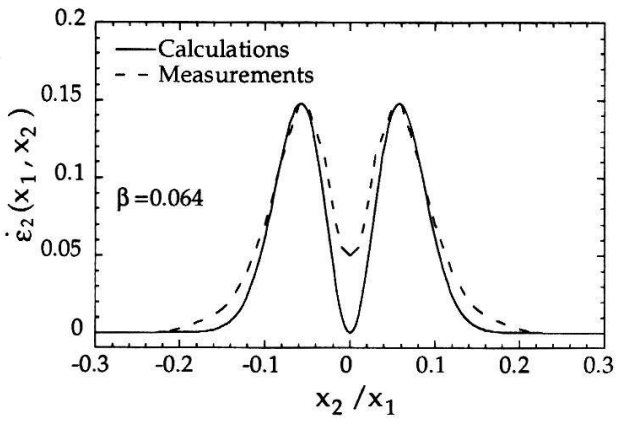

Figure 1: The scaled turbulent kinetic energy production in real space. The function, which has only been calculated with the relations between the brackets in equation (2), is compared with experimental results from Ref. [3]. The deviation (e.g. at the origin of the co-ordinate system) is caused by neglecting the two terms in equation (1).

The outlet velocity is denoted by u_0 and the core distance by x_0. For other symbols see Ref. [2]. The Fourier transform of (2) in cylindrical co-ordinates (x_1, x_2, x_3) is

$$\hat{\varepsilon}(k) = \int_{x_0}^{\infty} dx_1 \cdot \int_0^{\infty} x_2 \cdot dx_2 \int_0^{2\pi} dx_3 \exp\left[-ik_2 \cdot x_2 \cdot \cos(k_3 - x_3) - ik_3 \cdot x_3 \right] \cdot \dot{\varepsilon}(x_1, x_2, x_3). \tag{3}$$

Inserting equation (2) and performing some calculations leads to the following relation containing a Bessel function of order zero

$$\hat{\varepsilon} = (u_0 x_0)^3 \cdot \int_{x_0}^{\infty} \frac{dx_1}{x_1^4} \exp(-ik_1 x_1) \int_0^{\infty} x_2 dx_2 2\pi \cdot J_0(k_2 x_2) \left[\exp\left(-\frac{x_2^2}{b^2}\right) - \exp\left(-\frac{3}{2}\cdot\frac{x_2^2}{b^2}\right) \right]. \quad (4)$$

Continuing the calculations, after some steps the next equation is obtained

$$\hat{\varepsilon} = \pi \cdot \beta^2 \cdot u_0^3 \cdot x_0^3 \int_{x_0}^{\infty} \frac{dx_1}{x_1^2} \cdot \exp(-ik_1 \cdot x_1) \cdot \left[\exp\left(-\frac{k_2^2 \cdot b^2}{4}\right) - \frac{2}{3} \cdot \exp\left(-\frac{k_2^2 \cdot b^2}{6}\right) \right]. \quad (5)$$

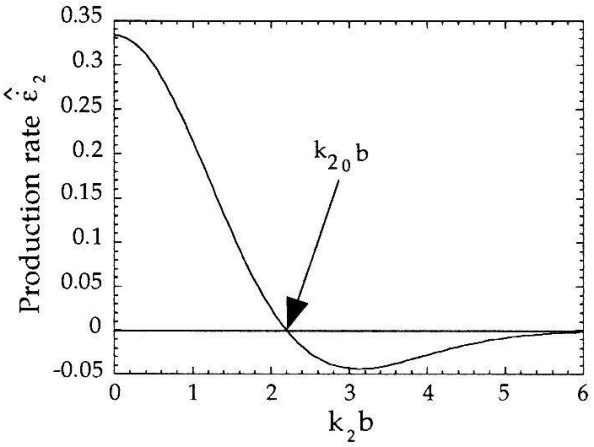

Figure 2: The Fourier transform of the turbulent kinetic energy production perpendicular to the center line of an axi-symmetric jet. Positive values at small wave numbers (large eddies) describe a transfer of energy from the mean velocity field to the turbulent fluctuations. At large $k_2 \cdot b$ the transport occurs in the opposite direction.

To determine the minimal size of the eddies with an energy gain, the zero of the Fourier transform in the radial direction

$$\hat{\varepsilon}_2(k_2; x_1) = 0 \quad (6)$$

is determined. This function $\hat{\varepsilon}_2$ is defined to be identical to the terms between the square brackets in equation (5). Then the corresponding wave length is

$$\lambda_{2_0} = \frac{2\pi}{k_{2_0}} = \frac{\pi}{\sqrt{3}} \cdot \frac{1}{\sqrt{\log_e\left(\frac{3}{2}\right)}} \cdot \beta \cdot x_1 \cong 2 \cdot \sqrt{2} \cdot \beta \cdot x_1 = 2 \cdot \sqrt{2} \cdot b. \quad (7)$$

Prandtl introduced the mixing length l and obtained a linear dependence on b [4], just as we have derived for the bounding wave length λ_{2_0}. At first he obtained a smaller factor, but later on he remarked that the mixing length must be larger. Therefore, we suggest that turbulent diffusion is strongly influenced by the eddies, which extract turbulent kinetic energy from the mean velocity field.

[1] J.O. Hinze, *Turbulence*, 2nd edition, McGraw-Hill, New York (1975).
[2] P.W. Egolf, Phys.Rev. E **49**, 1260 (1994).
[3] I. Wygnanski, H. Fiedler, J. Fluid Mech., **38**, 577 (1969).
[4] L. Prandtl, *Führer durch die Strömungslehre*, Vieweg-Verlag (1949).

Helv Phys Acta
Vol. 69, Separanda 1 (1996)

0018-0238/96/0100S11-02$1.50+0.20/0

TURBULENT ENERGY CASCADE MODEL INCLUDING INTERMITTENCY AND NON-EQUILIBRIUM ENERGY PRODUCTION AND DISSIPATION RATES

P.W. Egolf

Swiss Federal Laboratories for Materials Testing and Research, CH-8600 Dübendorf, Switzerland

D.A. Weiss

Laboratoire PMMH, École Supérieure de Physique et de Chimie Industrielles de la Ville de Paris,

F-75231 Paris, Cedex 05, France

An alternative energy cascade model based on less restrictions than Kolmogorov's model (published in 1941) is presented. The possibility of describing intermittency and a net production or dissipation rate of turbulent kinetic energy makes it useful for describing observed energy spectra and structure functions - which deviate significantly from Kolmogorov's results - e.g. newly presented measurements performed by Malerud, Måløy and Goldburg.

In 1941 Kolmogorov [1] published his model on homogenous isotropic turbulence, which leads to the experimentally verified -5/3 power law of the power spectrum [2]. The basic idea is an energy cascade of decaying eddies, with a conservative energy flux through the scales of an inertial range, formed by nonlinear redistribution of turbulent kinetic energy (see Fig.1).

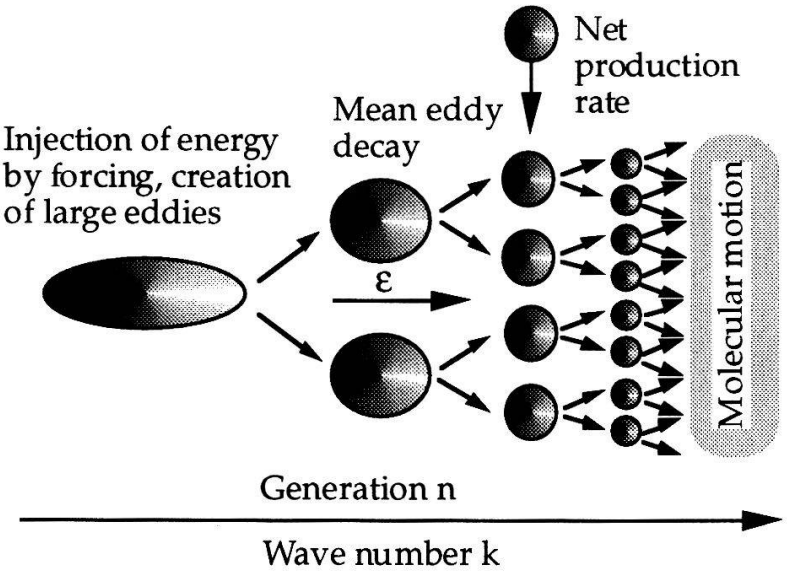

Figur 1: Turbulent kinetic energy cascade. Typical eddies of generation n, with corresponding wave number k_n, in the average decay toward the next larger wave number k_{n+1}.

Our aim is to apply these ideas to more complex flow problems.

For example, in mean shear flows of low or moderate Reynolds numbers large anisotropic eddies are created.

By the splitting process the anisotropy is assumed to decrease. Therefore, after a few generations approximately isotropic conditions are obtained. Furthermore, it is assumed that a net energy production or dissipation rate may occur. By considering the density ρ and energy transfer rate ε to be a function of the wave number k, these phenomena can be described. Then the following equation for the power spectrum is obtained

$$e(k) = \propto \rho(k)^{\frac{1}{3}} \cdot \varepsilon(k)^{\frac{2}{3}} \cdot k^{-\frac{5}{3}} \cdot \left(1 - \underbrace{\frac{1}{2} \cdot \frac{1}{\rho(k)} \cdot \frac{d\rho(k)}{dk} \cdot k}_{\text{Intermittency correction}} - \underbrace{\frac{1}{\varepsilon(k)} \cdot \frac{d\varepsilon(k)}{dk} \cdot k}_{\text{Non-equilibrium contribution}} \right). \quad (1)$$

The first term describes the Kolmogorv -5/3 power law. But now two additional contributions occur. The first is an intermittency correction, which is related to the space filling by the eddies. Experimentally it was found that in flows of finite Reynolds numbers usually smaller eddies are less space filling. The second non-equilibrium correction is related to a net energy production or dissipation rate.

Assuming scaling behaviour of the density ρ with exponent p and of ε with exponent q, the power spectrum is described by

$$e(k) = \propto (1 - \frac{1}{2}p - q) \cdot \rho_\pi^{\frac{1}{3}} \cdot \varepsilon_\delta^{\frac{2}{3}} \cdot k^{-\frac{5}{3}} \cdot \left(\frac{k}{k_\pi} \right)^{\frac{p}{3}} \cdot \left(\frac{k}{k_\delta} \right)^{\frac{2q}{3}}. \quad (2)$$

Equation (2) is completely compatible with Mandelbrot's investigation of intermittency leading to a spectral exponent -5/3+B [3]. By comparison it follows that B=p/3=(D-3)/3. D denotes the self similarity dimension, which is a special case of the fractal dimension. The quantity k_π has been introduced as injection wave number, and k_δ is the dissipation wave number.

When the exponents of the structure functions of order n are calculated, one obtains

$$\zeta_n = \frac{n}{3} + \frac{1}{3}(3-n) \cdot (3-D) - \frac{n}{3}q. \quad (3)$$

In the Kolmogorov limit (D=3, q=0) the first-order structure function is ζ_1=1/3. In plane Couette flow Malerud, Måløy and Goldburg [4] have measured scaling behaviour with an exponent 0.55 over a whole wave number decade. In the case D=2.5 with the alternative model this exponent can be described by q=1/3.

Herwejier and van de Water [5] have observed an exponent of the third-order structure function ζ_3, with a small but significant deviation from unity. The deviation can be qualitatively explained by the third term on the right of eq. (3).

In terms of the alternative model, considering S_3 and F_n, two complementary propositions on intermittent, non-equilibrium and anisotropic turbulence can be stated and proven. These shall be presented elsewhere.

[1] A.N. Kolmogorov, Doklady Akademii Nauk SSSR (N.S.) **30**, 299 (1941).
[2] H.L. Grant, R.W. Stewart and A. Moilliet, J. Fluid Mech. **12**, 241 (1962).
[3] B. Mandelbrot, *Turbulence and Navier-Stokes equation* (ed. R. Temam), Lecture Notes in Mathematics, vol. 565, Springer-Verlag, Berlin (1976).
[4] S. Malerud, K. J. Måløy and W. Goldburg, Phys. Fluids **7** (8), 1949 (1995).
[5] J. Herweijer and Willem van de Water, Phys. Rev. Lett. **74** (23), 4651 (1995).

Helv Phys Acta
Vol. 69, Separanda 1 (1996)

0018-0238/96/0100S13-02$1.50+0.20/0

Size-Effects in Hydrodynamics

R. Jaggi

Universidade do Algarve, U.C.E.H., Campus de Gambelas, 8000 Faro, Portugal

A model is presented in wich the Navier-Stokes equation is extended by introducing an adherence length $\lambda = \alpha^{-1}$. In a linearized approximation solutions for the laminar flow in a channel and in a tube of radius a are discussed; in the limit $\alpha a \ll 1$ the classical Hagen-Poiseuille flow is obtained. The friction force upon an infinitely long cylinder is given. For large systems (like oceans) the model provides an alternative to eddy-viscosities.

The Navier-Stokes equation for the drift velocity $\mathbf{v}$ of a normal incompressible fluid with density ρ and shear velocity coefficient η under pressure p is extended by a friction term, $\mathbf{F} = -\eta\alpha^2\mathbf{v}$, in analogy to an electron-fluid model for dc size-effect [1], where α is a constant characteristic of the fluid concerned and $\lambda = \alpha^{-1}$ is the "adherence length":

$$\rho\left(\frac{\partial \mathbf{v}}{\partial t} + (\mathbf{v}\nabla)\mathbf{v}\right) - \eta\left(\Delta\mathbf{v} - \alpha^2\mathbf{v}\right) = -\nabla p. \tag{1}$$

Omitting the non-linear convection term, Eq. (1) is simplified in the stationary case

$$\Delta\mathbf{v} - \alpha^2\mathbf{v} = \frac{\nabla p}{\eta}. \tag{2}$$

Eq. (2) is for the stationary flow v_z in an infinite channel of width $2a$

$$\frac{d^2 v_z}{dx^2} - \alpha^2 v_z = \frac{dp/dz}{\eta}. \tag{3}$$

The solution fulfilling the boundary condition $v_z(\pm a) = 0$ yields the velocity distribution

$$v_z(x) = v_0\left(1 - \frac{\cosh \alpha x}{\cosh \alpha a}\right) \tag{4}$$

with

$$v_0 = -\frac{dp/dz}{\eta\alpha^2}. \tag{5}$$

In the limit $\alpha a \ll 1$ the well-known parabolic profile of the standard theory independent of α is obtained

$$v_z(x) = -\frac{dp}{dz}\frac{a^2 - x^2}{2\eta}, \tag{6}$$

while in a deep channel, $\alpha a \gg 1$, there is a steep rise near the walls within a distance of the adherence length λ and in the bulk the velocity is nearly constant, $v_z = v_0$. Characteristic values for the oceans, $v_z = 10^{-1}\mathrm{m\ s^{-1}}$, $dp/dz = -10^{-3}\mathrm{Pa\ m^{-1}}$, $\eta = 10^{-3}\mathrm{Pa\ s}$ [2] are compatible with a constant $\alpha^2 = 10\ \mathrm{m^{-2}}$, $\lambda \approx 0.3$ m. So the model provides an alternative to the eddy viscosities wich depend on the coordinates and velocities.

For an infinitely long tube of radius a the stationary axial velocity v_z has to be determined by the inhomogeneous Bessel differential equation of zeroth order

$$\frac{d^2v_z}{dr^2} + \frac{1}{r}\frac{dv_z}{dr} - \alpha^2 v_z = \frac{dp/dz}{\eta} \tag{7}$$

with the solution fulfilling the boundary condition $v_z(\pm a) = 0$

$$v_z(x) = v_0\left(1 - \frac{\mathrm{I}_0(\alpha r)}{\mathrm{I}_0(\alpha a)}\right). \tag{8}$$

$\mathrm{I}_0(\alpha r)$ is the modified Bessel function of zeroth order. In the limit $\alpha a \ll 1$ the velocity distribution is parabolic

$$v_z(r) = -\frac{dp}{dz}\frac{a^2 - r^2}{4\eta} \tag{9}$$

and corresponds to the classical Hagen-Poiseuille law for laminar flow. For higher values of αa the profile becomes flat and finally for $\alpha a \gg 1$ a rectangular profile is approached.

Using Eq. (2) the force R per length upon an infinitely long cylinder of radius a in a fluid moving with velocity v_∞ can be calculated. The classical Navier-Stokes equation (where $\alpha = 0$) does not allow to define a friction coefficient in an infinitely two-dimensional fluid (Stokes-paradox) [3]. The exact solution of Eq. (2) in cylindrical coordinates yields

$$R = 4\pi\eta v_\infty \alpha^2 a^2 \left(1 - \frac{2\mathrm{K}_1(\alpha a)}{\alpha a \mathrm{K}_0(\alpha a)}\right) \tag{10}$$

where $\mathrm{K}_0(\alpha a)$ and $\mathrm{K}_1(\alpha a)$ are the modified Hankel functions of the zeroth and first orders, respectively. The asymptotic approximation for $\alpha a \gg 1$ is immediatly evident

$$R = 4\pi\eta v_\infty \alpha^2 a^2. \tag{11}$$

In the limit $\alpha a \ll 1$ there is

$$R = \frac{8\pi\eta v_\infty}{\ln(2/\alpha a) - C} \tag{12}$$

where $C = 0.577...$ is Euler's constant.

Eq. (12) can be compared with the result of Oseen's approximation [3]

$$R = \frac{8\pi\eta v_\infty}{2\ln(4/Re) - 2C + 1} \tag{13}$$

where the Reynolds number $Re = \rho a v_\infty/\eta$.

It can be shown that the present model provides good agreement with experiments in laminar flows with a constant adherence length. Also in the case of turbulence, where the role of the Reynolds number has to be discussed, analytic solutions of the linearized Eq. (1) allow the prediction of realistic velocity profiles.

References

[1] R. Jaggi, J. Appl. Phys. **69**, 816 (1991)

[2] J. P. Peixoto and A. H. Oort *Physics of Climate* (American Institute of Physics, 1992)

[3] J. D. Landau and E. M. Lifschitz *Fluid Mechanics* (Pergamon Press, 1992)

Helv Phys Acta
Vol. 69, Separanda 1 (1996)

0018-0238/96/0100S15-02$1.50+0.20/0

Quantum Interferometry: Some Basic Features Revisited

Markus Simonius

Inst. f. Teilchenphysik, Eidg. Techn. Hochschule, CH-8093 Zürich, Switzerland

The reduction paradigm of quantum interferometry is reanalyzed. In contrast to widespread opinion it is shown to be amenable to straightforward mathematical treatment within "every-users" simple-minded single particle quantum mechanics (without reduction postulate or the like), exploiting only its probabilistic content.

Consider a typical interferometer arrangement as sketched in Fig. 1. Its properties are well known: even if only one quantum (photon or neutron etc.) is inside the arrangement at a given time, the configuration of Fig. 1a can reveal interference between the states passing the two arms I and II provided none of them is blocked. Correspondingly, a pure single-particle state within the interferometer is represented by a normed wave function of the form

$$\varphi = c_1\varphi_1 + c_2\varphi_2, \quad \|\varphi\| = \|\varphi_1\| = \|\varphi_2\| = 1, \tag{1}$$

where, φ_1 and φ_2 represent states passing completely along one of the two paths I or II, respectively, in the interferometer and have zero component in the other (and thus are mutually orthogonal). For ideal 50:50 beam-splitting $|c_1|^2 = |c_2|^2 = \frac{1}{2}$, of course.

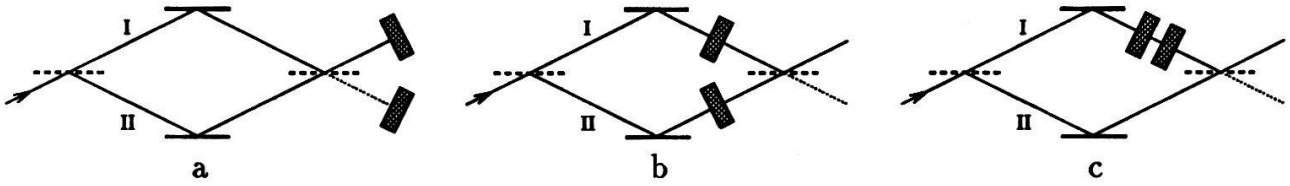

Figure 1: Sketch of typical interferometer arrangements with differently placed detectors.

Now consider instead coincidences between two detectors inserted into the two paths of the interferometer as shown in Fig. 1b. From the appearance of the wave function (1) one might suspect that such coincidences should occur. On the other hand, it is the fundamental proposition of quantum physics that quanta (particles or photons) are *indivisible entities* and thus a *single quantum* is not able to trigger both detectors in the arrangement of Fig. 1b (nor in Fig. 1a, of course). Though all this is much discussed textbook wisdom (tested also experimentally [3]), one looks in vain in the literature for a satisfying *derivation* of this fact which uses only the basic structure of single particle quantum theory and does not amount to just stating the fact as postulate in one way or another. But clearly it should be possible to deduce such basic properties mathematically once the general premises of the theory are laid down [1]. It is the object of this note to show that this is indeed so. Astonishingly, though the analysis to be presented is simple and straightforward, no such treatment is found in the literature, let alone in textbooks where it would belong.

For simplicity only pure states will be considered here explicitly, but the same results are obtained also directly from the general definition of superpositions in Ref. [2] which applies also to non-pure states (density operators).

Only the following minimal probabilistic set of postulates of quantum mechanics is used. No state reduction and no axiom of measurement etc.!

I Pure states are represented by normed elements $\varphi \in \mathcal{H}$ of a Hilbert space $\mathcal{H}$.

II The probability for a given kind of event for a system in a state represented by φ is given by an expectation value $\langle\varphi|A|\varphi\rangle$ where A is a hermitian operator on $\mathcal{H}$ which obviously must obey $0 \leq \langle\varphi|A|\varphi\rangle \leq 1$ for all $\varphi \in \mathcal{H}$, $\|\varphi\| = 1$.

The positivity postulate in II immediately leads to the following "silly" but far reaching **Theorem:** *Let A be a positive operator on $\mathcal{H}$ such that $\langle\psi_1|A|\psi_1\rangle = \langle\psi_2|A|\psi_2\rangle = 0$ for given $\psi_1, \psi_2 \in \mathcal{H}$. Then $\langle\psi|A|\psi\rangle = 0$ for all superpositions $\psi = c_1\psi_1 + c_2\psi_2$ between them.*

In order to apply this theorem to Fig. 1b with the two detectors in coincidence one only has to remark that one of the fundamental requirements for a coincidence between the two detectors is that the probability for a coincidence event be zero for any state which has zero component in one of the two arms of the interferometer, i.e if either $c_1 = 0$ or c_2=0 in eq. (1). (This is actually what careful experimenters check in order to verify that their arrangement does not produce spurious coincidence events!) Thus $\langle\varphi_1|A|\varphi_1\rangle = \langle\varphi_2|A|\varphi_2\rangle = 0$ where A is the operator describing the probability of coincidence events. It then follows from the above theorem that $\langle\varphi|A|\varphi\rangle = 0$ also for arbitrary $\varphi = c_1\varphi_1 + c_2\varphi_2$ and thus that *also for arbitrary superpositions between the states in the two arms of the interferometer the two detectors in Fig. 1b have zero probability to produce a coincidence event.*

Thus "what must be" is graciously born out by the mathematical analysis in spite of appearance of the wave function in eq. (1), "with nothing left to the discretion of the theoretical physicist" [1] (except to formulate the problems properly).

A corresponding "reduction theorem" is obtained similarly (using anticoincidence, this time) for an arrangement of the kind shown in Fig. 1c where now both detectors are in the same path and it is assumed that at least the first detector transmits (does not absorb) the quanta: If the two detectors have unit efficiency either both of them fire or none.

It is emphasized that postulate II is an integral part of the mathematical structure of quantum theory and not just a supplementary interpretation. In fact this postulate distinguishes quantum theory from classical wave theory.

The structure of the "silly" theorem on which this is based and of the corresponding physical statements is emphasized: Conclusions for arbitrary superpositions between two states φ_i are obtained from conditions imposed only for the two states φ_i themselves. There is no need to *postulate* what happens in the case of superpositions. The results presented depend exclusively on properties of the Hilbert space used to describe an elementary system and the operators acting on it. Indeed, in the case analyzed explicitly here, it suffices to take into account the two-dimensional space spanned by φ_1 and φ_2 in eq. (1) which supports only four linearly independent operators.

Two-slit or Stern-Gerlach arrangements can be analyzed correspondingly.

Of course, the features proved here must be revealed also if the detection devices or whatever are taken into account explicitly. However, against widespread opinion [4], it is definitely not *necessary* to do so let alone to invoke corresponding macroscopic properties.

References

[1] J. S. Bell, Physics World **3** No. 8, August 1990, p. 33.
[2] M. Simonius, Helv. Phys. Acta **66**, 721 (1993); **65**, 884 (1992).
[3] P. Grangier, G. Roger, and A. Aspect, Europhysics Letters **1**, 173 (1986).
[4] K. Gottfried, Physics World **4** No. 10, October 1991, p.34.

Helv Phys Acta
Vol. 69, Separanda 1 (1996)

0018-0238/96/0100S17-02$1.50+0.20/0

Relaxation of electrons in weakly-onedimensional semiconductor quantum wires mediated by LO-phonons

C. Ammann, M.-A. Dupertuis †, U. Bockelmann ‡, B. Deveaud †

Institute of Theoretical Physics, University of Lausanne, CH-1015 Lausanne,
†IMO, EPFL, CH-1015 Lausanne
‡WSI, Technische Universität, München

A weakly-onedimensional heterostructure is a quantum wire structure tailored so that the carriers are tightly confined in a direction, weakly confined in another and free to move in the third. The electronic bound states are computed using the envelope function approximation in the frame of the $k.p$ theory and the adiabatic approximation. Transition rates of the electrons from any bound state to any other bound state mediated by the LO-phonons are then evaluated. The lifetimes of excited levels and average energy with respect to time are computed.

A principal axis of development of electronic devices relies on including low-dimensional semiconductor heterostructures. Its motivation is the potential ability to tailor the electronic states and phase space. Enhanced transport properties, such as lower carrier scattering or higher mobility might be obtained; in the field of optics, the redistributed density of states and enhanced oscillator strengths are of interest. The optimization of such low-dimensional structures will provide faster and more economic devices.

As the radiative recombination is slower than any scattering process, we can consider that each kind of charge carriers, electrons or holes, relaxes to the bottom of its respective band before they recombine radiatively. A precise knowledge of the dynamics of the cooling[3] of the charge carriers is then necessary to predict the time dependence of the measurements of some luminescence experiments.

From the great variety of mediators taking part in the relaxation of the charge carriers, we have considered only the most likely, the LO-phonons, and we have restricted our study to electrons. This is justified because, compared to the electrons, the holes are heavier and, in our case, their band offset is smaller, so that their density of states is bigger and their subbands are closer together. Hence the relaxation of the holes is faster and does not limit the speed of the whole process.

To be as realistic as possible, we have chosen $Al_\delta Ga_{1-\delta}As/GaAs$ crescent-shaped quantum wires [1] or V-groove quantum wires [2] which have been fabricated and studied. These structures are called "weakly 1-D wires" which means that the carriers are strongly confined in one direction, z, weakly confined in another, x and free in the third, y, (translationnal symmetry) (see Fig. 1). The confinement is provided by the geometrical variation of the concentration δ of Al: the wire itself, of pure GaAs ($\delta = 0$), is surrounded by a substrate of high Al concentration δ_0. In some samples, δ_0 varies with the lateral position x in a step-like manner. Since the gap increases with the Al concentration, the electrons are confined in the wire. The wire is typically 20 nm thick at $x = 0$ and becomes progressively thinner in either x directions. Its characteristic width is of the order of 100 nm.

In the envelope function approximation, the periodic structure of the crystal lattice is not considered and the potential in the structure is given by the conduction band edge as a function of x and z. As the system is invariant under translation along y, the electronic wave functions will be plane waves in that direction giving rise to a parabolic dispersion. Exploiting the weakly 1-D character of the section of the wire, we use the adiabatic approximation which consists of a quasi-decoupling of the Schrödinger equation in x and z. The transverse equation is first solved for each x. This means that one has to solve a 1D equation for square-well potentials, the width of each well being the width of the wire at x. The x-dependent eigenvalues are then identified with a set of effective potentials along x, labelled by the z-quantum number m, and for each m the solution of the equation with respect to x is obtained numerically. The states are specified by three quantum numbers: the wave vector k_y in the y direction, m for the z direction and i for the x direction.

Even in a confined structure, it is a good approximation to use bulk LO-phonons as the mediators of the relaxation. Since the bulk LO-phonons are almost dispersionless, they connect electron states whose energies differ by exactly $\hbar\omega_{LO}$. The transition rates are computed using the Fröhlich interaction and the Fermi Golden Rule, and are the product of the density of the final electronic states and a matrix element $< fin|\exp(-\mathrm{i}(q_x x + q_z z))|in >$ $/|q|$ where $|in >$ and $|fin >$ are the initial and final electronic states and q is the phonon wave vector. As the density of states behaves like $E^{-1/2}$ in a 1-D structure, where E is the kinetic energy, the rates present singularities when the final state lies at a subband edge, and decrease monotonically as a function of E. It can be seen that pairs of states with large overlap integrals have strong rates and that the intrasubband relaxation is always the shortest away from resonances. Typical rates are of the order of a picosecond. The lifetimes of initial states are obtained from the sum of the rates to all the final accessible states.

We have considered global cascades of disintegration and computed the average energy of a single electron initially placed in a given subband, as a function of time. If the energetic splitting between the subband edges is small ($\simeq$ 5 meV), many different channels open, and resonances are frequent. The time needed to relax down to the ground subband and attain an energy smaller than $\hbar\omega_{LO}$, is of the order of 10^{-13} s, which is very fast. The global time increases with the initial energy E, but jumps down at every $\hbar\omega_{LO}$ above subband edges where new channels open.

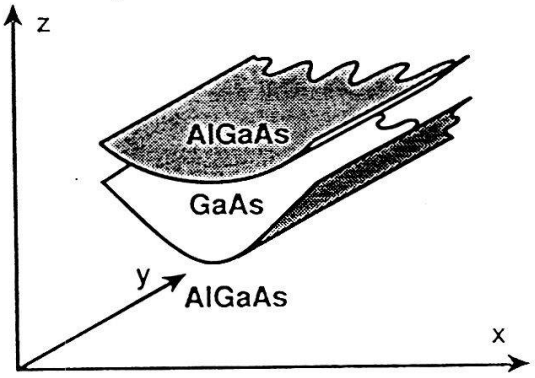

Fig. 1

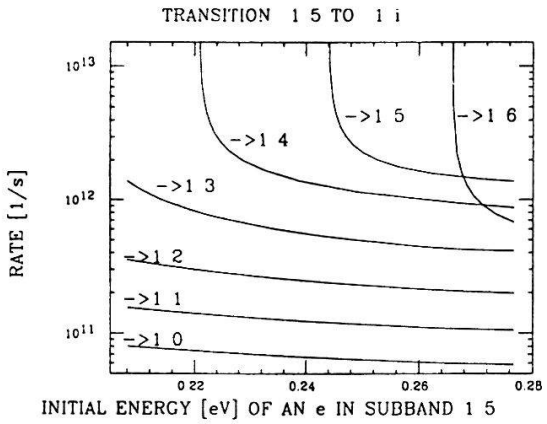

Fig. 2 →

References

[1] A.C. Maciel, C.Kiener, L.Rota, J.F.Ryan, U.Marti, D.Martin, F.Morier-Genoud, F.K.Reinhart, Appl. Phys. Lett. 66(22), pp.3039-3041 (1995)

[2] E.Kapon, D.M.Hwang, and R.Bhat, Phys. Rev. Lett. 63(4), p.430 (1989)

[3] N.S. Mansour, J.P. Leburton et al., Appl. Phys. Lett. 67, p.3480 (1995)

Helv Phys Acta
Vol. 69, Separanda 1 (1996)

0018-0238/96/0100S19-02$1.50+0.20/0

An Explanation for the Discrepancies between the Experimental Muonic Capture Ratios A(Ar,Ne)

Y.-A. Thalmann, R. Jacot-Guillarmod, F. Mulhauser, L.A. Schaller, L. Schellenberg, H. Schneuwly, S. Tresch and A. Werthmüller

Institut de Physique de l'Université, CH-1700 Fribourg, Suisse

The determination of muon capture ratios in elements requires a particular attention to the time distribution of the measured muonic X-rays. Different cuts in time distributions allow to explain the discrepancies between the five capture ratios A(Ar,Ne) published in the literature.

Atomic capture ratios A(Z,Z') of negative muons have been measured in many solid compounds $Z_nZ'_m$ and gaseous mixtures for the past thirty years using muonic X-ray yields. Moreover, results published by different groups for a same capture ratio often disagree with each other. Such discrepancies also exist for elements without chemical bonds such as neon and argon.

By performing measurements of the capture ratio A(Ar,Ne) in 1:1 mixtures of Ar + Ne, we expected to find correlations between the different values and various experimental conditions. However, our measured ratios obtained from different experimental conditions agreed all with each other and scattered around a mean value of 1.28(3) which disagrees with almost all others [1,2]. Our analysis revealed the importance of the time distributions of the detected muonic X-rays in the determination of the capture ratio.

In a usual experimental set-up, muons entering the target vessel are detected by a scintillator. To be recorded, the signal of the X-ray detector has to be in coincidence with a signal from the entrance scintillator. Traditionally, coincidence widths of about 50 ns were chosen (see e.g. Ref. [3]). In our set-up, we measure the time interval between the two signals. Thus, each event recorded includes a time information besides the energy information. The time spectra of the muonic transitions can be reconstructed off-line by setting windows in the corresponding energy spectrum. They have in good approximation a gaussian shape whose centroids and full widths at half maximum depend on the energy of the transition. It can however occur that these peaks are shifted during a measurement, or that a second and much smaller peak due to the electronic processing of the signals appears.

Without the complete information provided by the time spectra, it could happen that part of the good events were cut because of the chosen coincidence window. We have studied this phenomenon by setting a time window of 60 ns on the $2p - 1s$ transitions in argon and in neon. The intensities of both these transitions represent approximately 90% of the total intensity of the Lyman series and can hence be used to determine the capture ratio. We

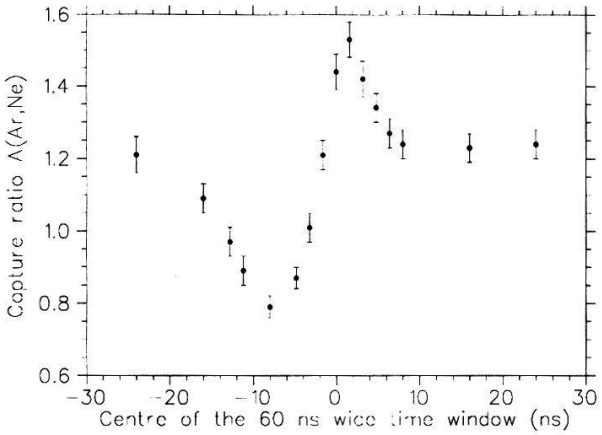

Figure 1: Experimental capture ratios A(Ar,Ne) determined by varying the position of the time window around time $t = 0$ which is defined by the mean value of the centroids of both argon and neon $\mu(2p - 1s)$ peaks. The data used are those of a measurement of a gaseous mixture of 1:1 Ar + Ne at 15 bar.

have then moved the time window, built the corresponding energy spectra and determined the capture ratio A(Ar,Ne) for various positions. The results are shown in figure 1. With this method, the four other published capture ratios A(Ar,Ne) measured in 1:1 mixtures, namely 1.01(3), 1.11(14), 1.41(7) and 1.64(6) (see Ref. [3]) can be reproduced.

References

[1] Y.-A. Thalmann *et. al.*, in *Muons and Pions in Matter*, ed. by T.N. Mamedov and V.N. Duginov, JINR, Dubna (1995), p. 151.
[2] Y.-A. Thalmann *et. al.*, Helv. Phys. Acta **66**, 895 (1993).
[3] P. Ehrhart *et. al.*, Z. Phys. A - Atoms and Nuclei **311**, 259 (1983).

Helv Phys Acta
Vol. 69, Separanda 1 (1996)

0018-0238/96/0100S21-02$1.50+0.20/0

Fractals in isotropic systems generated with attracting spheres

Erich Stoll[1], Christian Stern[2] and Peter Stucki[2]

[1]Physik-Institut, Universität Zürich-Irchel, Winterthurerstr. 190, CH-8057 Zürich, [2]Institut für Informatik der Universität Zürich, MultiMedia Laboratorium, Winterthurerstr. 190, CH-8057 Zürich

Isotropic non-crystal fractal systems are generated using the technique of simulated annealing and frozen Lennard-Jones fluids. From all nearest neighbor bonds shorter than 1.15σ, a subset is selected randomly with the probability $p \approx p_c$. Afterwards, bond-percolation clusters are searched for. Applying the box-counting method, the fractal dimension D is 2.58 ± 0.015, and by fitting the slope of the static structure factor S(q), D is 2.40 ± 0.02. Both values are close to that of a fractal system on a three-dimensional lattice.

In the past, computer simulations of fractals have often been performed on lattice systems [1-3]. The majority of fractal objects, e.g. silica aerogels [4], have no lattice periodicity. Therefore, alternative methods for generating isotropic non-crystal fractals are important.

150 particles with randomly chosen coordinates are enclosed in a cubic box with a side length of 6σ. They interact with the Lennard-Jones potential

$$V(r) = 4\epsilon[(\frac{\sigma}{r})^{12} - (\frac{\sigma}{r})^{6}]. \quad (1)$$

Periodic boundary conditions are used. The time integration is done by the Verlet algorithm [5]. By simulated annealing, amorphous or glassy states are generated [6].

To increase the box-size, the original box is concatenated in all three space dimensions with its replica. Connecting bonds are defined if distances between corresponding neighboring particles are shorter than a threshold of 1.15σ. A subset is selected randomly with the probability $p \approx p_c$. With the bond-percolation cluster-counting algorithm [4,8] percolation clusters containing N particles are searched for. This procedure is repeated with different random numbers to obtain reasonable statistics. Using the box-counting method [8], the occupancy $\overline{N}$ for large boxes is given by $\lim_{\overline{N}\to\infty} \overline{N} \propto l^{\mathrm{D}}$. For the isotropic system, $p = 0.3825 \approx p_c$ and box-side lengths l between 6σ and 48σ the occupancy curve is plotted in Fig. 1 (open circles followed by long dashes) as $l^{2.580\pm0.015}$. The three-dimensional cubic lattices [3] with side lengths between 1 and 30 inter-particle distances are shown by full circles followed by short dashes, $l^{2.537\pm0.037}$.

For $p = p_c$ the static structure factor $S(q)$ (the Fourier transformation of the two particle correlation function) decays as [2,3] $S(q) \propto q^{-\mathrm{D}}$, or $S(q) = \frac{1}{N}|\sum_{j=1}^{N} \exp i\vec{x}_j\vec{q}|^2$. For larger q-values, the deviation of S(q) from the slope line in the lattice system (with short dashes) is comparable to that of the two-dimensional bond percolation system [3]. In the isotropic system, an increase of S(q) towards large q-values is visible as a precursor of the first peak in the structure factor of liquids or amorphous states. For the simple cubic lattice, the slope is

$q^{-2.41\pm0.02}$ (short dashes) and for the isotropic system $q^{-2.40\pm0.02}$ (long dashes). The fractal dimensions of both systems are nearly equal.

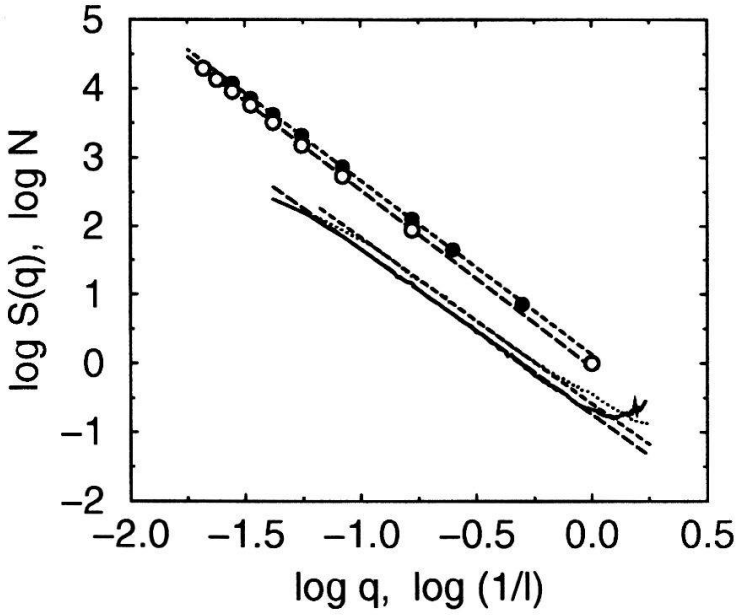

Figure 1: $\overline{N}(1/l)$ (circles) and S(q) of the isotropic (solid curve) and the lattice system (dotted curve). $1/l$ and $q/2\pi$ are in units of $1/\sigma$ for the isotropic and $1/a$ for the lattice system. a denotes the next nearest neighbor distance. The fitted straight lines are with long dashes and short dashes. 200 different random-number chains are used for the calculation of S(q) in the isotropic system with the box-length of 48σ and 100 chains in the lattice system with the box-length of $30a$.

Lattice-free and isotropic fractal systems can be generated using molecular dynamics simulations [6]. The isotropic interaction between particles is responsible for a rather compact packing, and the fractal dimension D evaluated with box-counting is 2.580 ± 0.015 and from the decay of S(q) 2.40 ± 0.02. Both values are comparable to the ones of a three-dimensional lattice.

We are grateful to the Swiss National Science Foundation, Priority Program Computer Science, for financial support.

References

[1] M.L. Williams and H.J. Maris, Phys. Rev. B**31**, 4508 (1985).
[2] E. Courtens, R. Vacher, and E. Stoll, Physica D**38**, 41 (1989).
[3] Erich Stoll, Max Kolb, and Eric Courtens, Phys. Rev. Lett. **68**, 2472 (1992).
[4] J. Fricke, Phys. Bl. **51**, 935 (1995).
[5] L. Verlet, Phys. Rev. **159**, 98 (1967).
[6] Christian Stern, Peter Stucki, and Erich Stoll, *Priority Programme Information Research*, Proc. Information Conf. Module 3 Mass. parall. syst., eds. K. Bauknecht and J.M. Grossenbacher, (Swiss Nat. Sci. Fond., Bern, 1994), pg. 29.
[7] E. Stoll and C. Domb, J. Phys. A: Math. Gen. **12**, 1843 (1979).
[8] E.P. Stoll and M. Kolb, Physica A**185**, 222 (1992).

Helv Phys Acta
Vol. 69, Separanda 1 (1996)

0018-0238/96/0100S23-02$1.50+0.20/0

Thermally Assisted Flux Flow Excited by Ultrasound in Superconducting Thin Films

Y. Horie[a,b], T. Oku[b], T. Nomiyama[b], T. Miyazaki[b] and L. Rinderer[a]

[a]Institut de Physique Expérimentale, Université de Lausanne, CH-1015 Lausanne
[b]Dept. of Electrical & Electronics Engineering, Kagoshima Univ., Kagoshima 890, Japan

A new ultrasonic method has been proposed for the study of flux pinning properties in high T_c superconducting thin films. The depinned flux lines excited by the ultrasound are detected as the excess flux flow voltage. A maximum of the voltage, which was observed below T_c, is explained qualitatively by considering ultrasonic attenuation due to the thermally assisted flux flow.

Since the existence of magnetic irreversibility was revealed for high T_c superconductors (HTSC) by Müller *et al.*[1], various experimental and theoretical studies concerning the unusual properties of flux lines (FL's) have been reported for many kinds of samples.

Among the experimental methods for the study of the flux pinning properties, an ultrasonic method is superior to the others in some points. One of the superior points is that the effect of the sample shape and the grain boundary can be neglected. When FL's are pinned rigidly, FL's are vibrated by ultrasound through the vibration of pinning centers in the crystal. Thus, all pinned FL's in the sample are vibrated by ultrasound, while in ac susceptibility measurements, for instance, only FL's near the surface and the grain boundary are vibrated because of the shielding of ac magnetic field. The ultrasonic method should be useful for samples such as thin films for which the demagnetizing effect is not negligible.

Near the depinning temperature, since a part of ultrasonic energy is dissipated to excite FL's from the pinning potential, the attenuation of ultrasound becomes maximum [2]. For thin films, however, the change in the attenuation coefficient α of bulk ultrasound is too small to detect. In this study, we attempted to measure not α but the voltage induced by the flow of depinned FL's.

The outline of the method is shown in Fig.1 [3]. The composite of a thin film and a substrate resonates with the longitudinal ultrasound of $f_0 = 32.6$ MHz, and FL's pinned in the thin film are vibrated from side to side. In this configuration, the amplitude of the ultrasound and the displacement of FL's are the maximum in the center of the film. Therefore, the deformation of FLL is equivalent to that produced by the ultrasound standing along the film and polarizing to y-axis.

When an electrical current is applied to the x-direction, a collective flux flow occurs in the direction of Lorentz force. Therefore, from the difference of the flow voltage with and without ultrasound, we can detect the influence of the

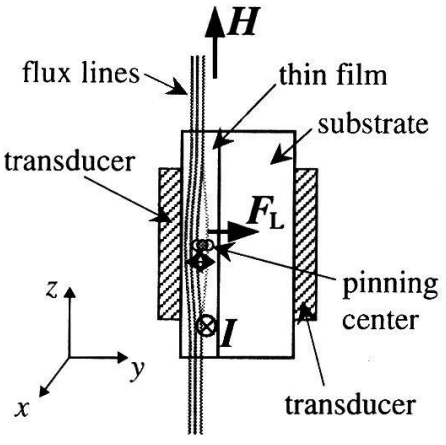

Fig.1 Interaction between ultrasound and FL's in a thin film.

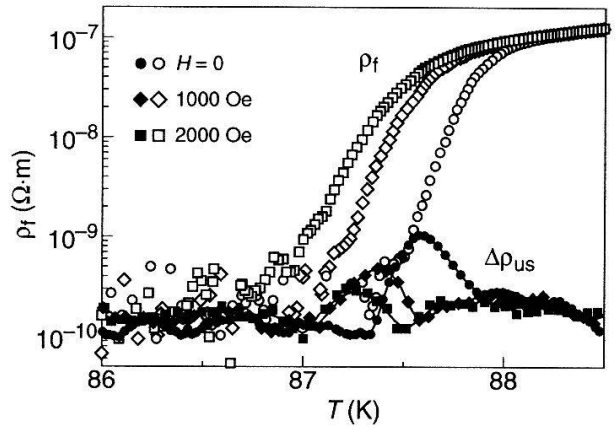

Fig.2 Temperature dependence of ρ_f and $\Delta\rho_{us}$.

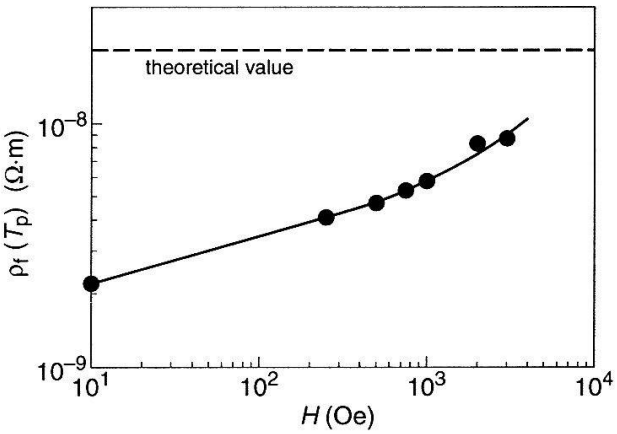

Fig.3 Magnetic field dependence of $\rho_f(T_p)$.

ultrasonic excitation on FL's. To detect only the small excess voltage produced by ultrasound, the ac component of flux flow resistivity, $\Delta\rho_{us}$, was detected by applying ultrasound amplitude-modulated with a frequency, $f_{AM} = 1$ kHz.

Figure 2 shows the temperature dependence of $\Delta\rho_{us}$ and resistivity ρ_f for a $YBa_2Cu_3O_{7-\delta}$ thin film of which c-axis is normal to the film. Near the resistive transition, a peak was observed in $\Delta\rho_{us}(T)$. According to the theory[3] in which the thermally assisted flux flow (TAFF)[4] and the excitation of FL's due to ultrasound[2] are taken into account, the peak in $\Delta\rho_{us}(T)$ appears when ρ_f is comparable to the quantity determined by the ultrasonic frequency f and the wave length λ, *i.e.* $\rho_f = \mu_0 f\lambda/2\pi$. By putting experimental values of $f = f_{AM} = 1$ kHz and $\lambda = 10^{-2}$ m, we get the flow resistivity of $\rho_f(T_p) = 2.0 \times 10^{-8}$ Ω·m at the peak temperature T_p. Figure 3 shows the magnetic field dependence of the resistivity $\rho_f(T_p)$ determined by the experimental results shown in Fig.2. As seen, the magnitude of $\rho_f(T_p)$ approaches the theoretical value with increasing magnetic field. Although we also measured the f_{AM} dependence of T_p, it was much weaker than the theoretical prediction.

Most of the reason of the above-mentioned discrepancies with the theory should be attributed to the serious distortion of FLL, since the lattice spacing of FLL is comparable to the film thickness in the low field region of the experiments. It is sufficiently large media that was taken into consideration in the theory. Besides, the theory is based on the thermal diffusion of FL's in which a sufficiently large numbers of FL's are assumed to move diffusively so as to release the deformation of FLL produced by ultrasound. In the experiments with $\boldsymbol{H} \parallel ab$-plane, the FL's are pinned strongly. Therefore, the TAFF regime with linear I-V characteristics which was treated in the theory is narrow in the H-T plane, and most of the region is attributed to the flux creep regime with non-linear I-V curves.

To confirm the above speculation, it is necessary to make simultaneous measurements of $\Delta\rho_{us}$ and the I-V characteristics in a wide range of I and H. Besides, with the configuration $\boldsymbol{H} \parallel c$-axis in which the pinning potential is small and the TAFF region is wide, we can examine the validity of the experiments proposed in this paper.

References

[1] K. A. Müller *et al.*, Phys. Rev. Lett. 58, 1143 (1987).
[2] J. Pankert, Physica C 168, 335 (1990).
[3] Y. Horie *et al.*, *to be published in* Physica C 258, (1996).
[4] P. W. Anderson and Y. B. Kim, Rev. Mod. Phys. 36, 39 (1964).